

SCIENTIFIC REPORTS

OPEN

Formation of novel transition metal hydride complexes with ninefold hydrogen coordination

Received: 14 December 2016

Accepted: 03 February 2017

Published: 13 March 2017

Shigeyuki Takagi¹, Yuki Iijima¹, Toyoto Sato¹, Hiroyuki Saitoh², Kazutaka Ikeda³, Toshiya Otomo³, Kazutoshi Miwa⁴, Tamio Ikeshoji¹ & Shin-ichi Orimo^{1,5}

Ninefold coordination of hydrogen is very rare, and has been observed in two different hydride complexes comprising rhenium and technetium. Herein, based on a theoretical/experimental approach, we present evidence for the formation of ninefold H-coordination hydride complexes of molybdenum ($[\text{MoH}_9]^{3-}$), tungsten ($[\text{WH}_9]^{3-}$), niobium ($[\text{NbH}_9]^{4-}$) and tantalum ($[\text{TaH}_9]^{4-}$) in novel complex transition-metal hydrides, $\text{Li}_5\text{MoH}_{11}$, $\text{Li}_5\text{WH}_{11}$, $\text{Li}_6\text{NbH}_{11}$ and $\text{Li}_6\text{TaH}_{11}$, respectively. All of the synthesized materials are insulated with band gaps of approximately 4 eV, but contain a sufficient amount of hydrogen to cause the H 1s-derived states to reach the Fermi level. Such hydrogen-rich materials might be of interest for high-critical-temperature superconductivity if the gaps close under compression. Furthermore, the hydride complexes exhibit significant rotational motions associated with anharmonic librations at room temperature, which are often discussed in relation to the translational diffusion of cations in alkali-metal dodecahydro-*closo*-dodecaborates and strongly point to the emergence of a fast lithium conduction even at room temperature.

Although exhibiting the simplest form, hydrogen has an exceptionally rich chemistry, forming various chemical bonds in materials¹. The flexibility of hydrogen is the source of many interesting functionalities in hydrides, such as hydrogen storage², superconductivity^{3–6}, fast ionic conductivity⁷, magnetism⁸ and metal–insulator transition^{9,10}; thus, materials containing a large amount of hydrogen are promising candidates not only for improving material performance but also for the emergence of latent functionalities.

Complex transition metal hydrides represent a class of hydrogen-rich materials, wherein a number of H atoms covalently bind to a transition metal element (*T*) to form hydride complexes with a remarkably rich variety of H-coordination modes ranging from twofold to ninefold^{11–25}. These complexes are stabilized by charge transfer from electropositive counterions, such as alkali and alkaline earth metals, to form insulating hydrides^{1,20,23}. In general, the H-coordination number increases from right to left along a given period because of the trend of increasing atomic size, which allows more hydrogen binding. At the same time, despite research spanning the past several decades, the elements capable of forming hydride complexes are thought to be limited to those in Groups 7–12¹⁸. This limitation has so far precluded further discovery of hydride complexes with high H-coordination. For example, the presently known members with the ninefold H-coordination are limited to those comprising the Group 7 elements technetium ($[\text{TcH}_9]^{2-}$)¹¹ and rhenium ($[\text{ReH}_9]^{2-}$)^{12–14,16,17}. However, we recently reported the formation of the first Group 6 hydride complex $[\text{CrH}_7]^{5-}$ in Mg_3CrH_8 ²⁵, thereby demonstrating that there is no *a priori* reason for this limitation and paving the way for the discovery of higher H-coordination hydride complexes comprising unexplored elements to the left of Group 7.

To demonstrate the feasibility of this strategy, we have experimentally examined the formation of novel transition metal hydride complexes of Group 5 and Group 6 elements (Mo, W, Nb and Ta) based on a first-principles prediction. Lithium was selected as a counterion because of its low electronegativity, which is expected to thermodynamically stabilize the complex hydride phases^{1,20,23}. The crystal structures and electronic structures of the

¹Institute for Materials Research, Tohoku University, Sendai 980-8577, Japan. ²Quantum Beam Science Research Directorate, National Institute for Quantum and Radiological Science and Technology, Hyogo 679-5148, Japan.

³Institute of Materials Structure Science, High Energy Accelerator Research Organization, Tsukuba 305-0801, Japan.

⁴Toyota Central R&D Laboratories, Inc., Nagakute 480-1192, Japan. ⁵WPI-Advanced Institute for Materials Research, Tohoku University, Sendai 980-8577, Japan. Correspondence and requests for materials should be addressed to S.O. (email: orimo@imr.tohoku.ac.jp)

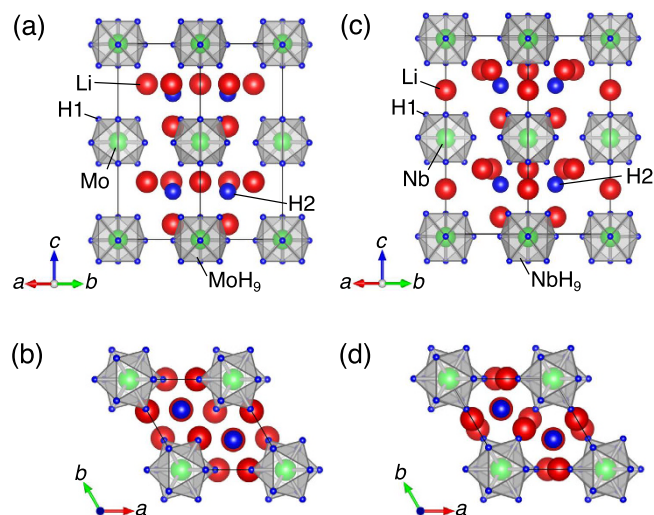


Figure 1. Crystal structures. (a–d) Density functional theory (DFT) structures of $\text{Li}_5\text{MoH}_{11}$ (a,b) and $\text{Li}_6\text{NbH}_{11}$ (c,d) viewed along the [110] (a,c) and [001] (b,d) directions. $\text{Li}_5\text{WH}_{11}$ and $\text{Li}_6\text{TaH}_{11}$ have isostructures to $\text{Li}_5\text{MoH}_{11}$ and $\text{Li}_6\text{NbH}_{11}$, respectively.

Hydrogenation reaction	ΔH_f (kJ/mol)	ΔS_f (J/mol·K)
$5\text{LiH} + \text{Mo} + 3\text{H}_2 \rightarrow \text{Li}_5\text{MoH}_{11}$	−105	−254
$5\text{LiH} + \text{W} + 3\text{H}_2 \rightarrow \text{Li}_5\text{WH}_{11}$	−128	−264
$6\text{LiH} + \text{NbH}_{0.65} + 2.175\text{H}_2 \rightarrow \text{Li}_5\text{MoH}_{11}$	−91	−120
$6\text{LiH} + \text{TaH}_{0.65} + 2.175\text{H}_2 \rightarrow \text{Li}_5\text{TaH}_{11}$	−117	−151

Table 1. Enthalpy changes ΔH_f and entropy changes ΔS_f of the conceivable hydrogenation reactions.

obtained samples were investigated using a combination of experimental and *ab initio* approaches. Finally, we discuss the prospects for the emergence of H-driven functionalities in the obtained materials.

Results

First-principles predictions. We first performed a ground-state structure search of Li–Mo–H and Li–Nb–H systems using first-principles calculations. Figure 1 shows the obtained most stable structures found with stoichiometries of $\text{Li}_5\text{MoH}_{11}$ and $\text{Li}_6\text{NbH}_{11}$. In $\text{Li}_5\text{MoH}_{11}$, nine H atoms (H1) form a tricapped trigonal prism around the Mo atoms sitting at the (0, 0, 0) and (0, 0, 1/2) coordinates of the hexagonal lattice and two isolated H atoms (H2) are located at the approximate centres of the trigonal prisms formed by the six Mo atoms. The four Li atoms coordinate to the H2 atoms, forming a two-dimensional network of corner-sharing tetrahedra between the layers of MoH_9 units. $\text{Li}_6\text{NbH}_{11}$ has a structure similar to that of $\text{Li}_5\text{MoH}_{11}$; however, it has an additional Li site between the NbH_9 tricapped trigonal prisms along the *c*-axis, which accommodates the 6:1 stoichiometry between Li and Nb.

The calculated standard heats of formation ΔH_f° are -510 kJ/mol for $\text{Li}_5\text{MoH}_{11}$ and -637 kJ/mol for $\text{Li}_6\text{NbH}_{11}$, which are much lower than those of the conceivable decomposed products, $5\text{LiH} + \text{Mo} + 3\text{H}_2$ and $6\text{LiH} + \text{NbH}_{0.65} + 2.175\text{H}_2$, respectively; therefore, the materials could potentially be synthesized via the following reactions: $5\text{LiH} + \text{Mo} + 3\text{H}_2 \rightarrow \text{Li}_5\text{MoH}_{11}$ and $6\text{LiH} + \text{NbH}_{0.65} + 2.175\text{H}_2 \rightarrow \text{Li}_5\text{MoH}_{11}$, with the enthalpies of reaction ΔH_r of -105 and -91 kJ/mol, respectively (note that we used -81 kJ/mol²⁶ for LiH and -60 kJ/mol for $\text{NbH}_{0.65}$ ²⁷). We observed that the isostructural *5d* analogues $\text{Li}_5\text{WH}_{11}$ and $\text{Li}_6\text{TaH}_{11}$ also have higher thermodynamic stabilities of -529 and -651 kJ/mol with respect to the conceivable decomposition products $5\text{LiH} + \text{W} + 3\text{H}_2$ and $6\text{LiH} + \text{TaH}_{0.65} + 2.175\text{H}_{0.65}$, respectively (note that the enthalpies of reaction are estimated to be -128 and -117 kJ/mol, respectively, using -51 kJ/mol for $\text{TaH}_{0.65}$ ²⁸). The results are summarized in Table 1.

Electronic structures. Based on the obtained structures, we discuss the electronic structures. Figure 2 shows the calculated electronic densities of states (DOSs) and the H *s* and *T spd* projections. We checked for magnetic states and observed no magnetic ordering in any of the materials.

The most important feature of the electronic structures is that the 1s states of the nine H1 atoms forming the TH_9 tricapped trigonal prisms reach the Fermi level (E_F) in all materials, as observed in the third panels from the top in Fig. 2a–d. These states strongly hybridize with the *T spd* states to form the σ -bonds, which is evident from the H1 *s* and *T spd* characters of both the valence and conduction bands. These results are consistent with a previous electronic structure calculation by Singh *et al.*²⁹ for BaReH_9 , which contains the hydride complex ReH_9 . Because all nine bonding states are fully occupied by 18 electrons per formula unit, the TH_9 units can be considered as the hydride complexes $[\text{MoH}_9]^{3-}$, $[\text{WH}_9]^{3-}$, $[\text{NbH}_9]^{4-}$ and $[\text{TaH}_9]^{4-}$. The 1s states of the isolated H2 atoms

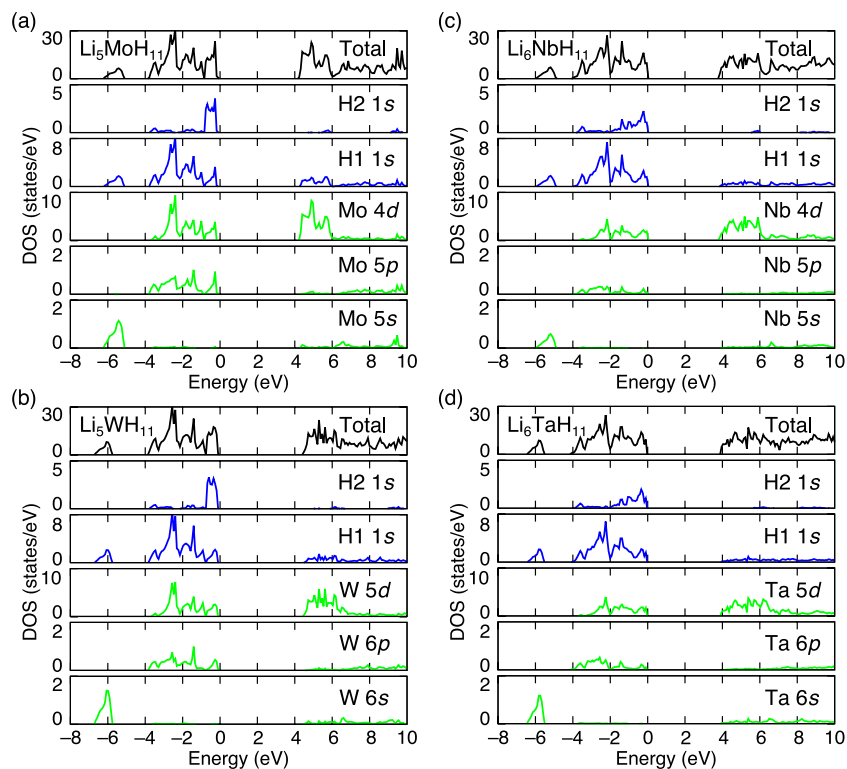


Figure 2. Electronic structures. Total electronic density of states (DOS; top panels) and H2 1s (second panel from the top), H1 1s (third panel from the top), *Td* (third panel from the bottom), *Tp* (second panel from the bottom) and *Ts* (bottom panels) projections for $\text{Li}_5\text{MoH}_{11}$ (a), $\text{Li}_5\text{WH}_{11}$ (b), $\text{Li}_6\text{NbH}_{11}$ (c) and $\text{Li}_6\text{TaH}_{11}$ (d). The energy zero is set at the valence-band maximum.

lie immediately below E_F without noticeable hybridization with any other states, as observed in the second panels from the top in Fig. 2a–d. Thus, these atoms can be considered as H^- ions. The electropositive Li states occur far above E_F (not shown) and donate one electron per atom to the hydride complexes to become Li^+ cations. Thus, we conclude that the ionic configurations of the current materials are $[\text{Li}^+]_5[\text{MoH}_9]^{3-}[\text{H}^-]_2$, $[\text{Li}^+]_5[\text{WH}_9]^{3-}[\text{H}^-]_2$, $[\text{Li}^+]_6[\text{NbH}_9]^{4-}[\text{H}^-]_2$ and $[\text{Li}^+]_6[\text{TaH}_9]^{4-}[\text{H}^-]_2$. The band gaps are approximately 4 eV in all of the materials.

Syntheses. We experimentally examined the possibility of the formation of the theoretically predicted complex transition metal hydrides using a high-pressure and high-temperature technique. Powdered mixtures of LiH and Group 5 and Group 6 transition metals were hydrogenated under 5 GPa at 923–1023 K for 24–48 h. The colours of the samples recovered at ambient pressure and temperature were yellow for Li–Mo–H, greenish yellow for Li–W–H, light grey for Li–Nb–H and white for Li–Ta–H, implying the insulating character, as is typical with complex transition-metal hydrides.

The recovered samples were characterized by Raman spectroscopy, and the results are illustrated in Fig. 3a–d (black lines) along with the density functional theory (DFT) spectra (red lines) calculated using a method reported in the literature³⁰. Because the primitive cells of $\text{Li}_5\text{MoH}_{11}/\text{Li}_5\text{WH}_{11}$ and $\text{Li}_6\text{NbH}_{11}/\text{Li}_6\text{TaH}_{11}$ comprise 34 and 36 atoms, respectively, there are a total of 99 ($10A_1 + 6A_2 + 6B_1 + 11B_2 + 17E_2 + 16E_1$) and 105 ($11A_1 + 6A_2 + 6B_1 + 12B_2 + 18E_2 + 17E_1$) zone-centre optical phonon modes, respectively, as represented by the tick marks in Fig. 3a–d. Among them, 76 modes ($10A_1 + 17E_2 + 16E_1$) of $\text{Li}_5\text{MoH}_{11}/\text{Li}_5\text{WH}_{11}$ and 81 modes ($11A_1 + 18E_2 + 17E_1$) of $\text{Li}_6\text{NbH}_{11}/\text{Li}_6\text{TaH}_{11}$ are Raman active. These modes provide an intense and asymmetric band at approximately $1660\text{--}1860\text{ cm}^{-1}$ and a weak band at approximately 1000 cm^{-1} in all the DFT spectra, which originate from the *T*–H stretching and H–*T*–H bending vibrations, respectively. The experimental spectra exhibit very similar features to those obtained by the DFT calculations, strongly supporting the formation of the theoretically predicted ninefold H-coordination hydride complexes.

Figure 3e–h shows X-ray diffraction (XRD) profiles of the recovered samples (black lines) and the profiles simulated based on the DFT structures (red lines). Although the samples contain small amounts of impurities, the Bragg peaks were well indexed to a similar hexagonal lattice with the lattice parameters listed in Table 2. While all of the Bragg peaks are considered to primarily originate from diffraction by the transition metals due to the small atomic scattering factors of H and Li, we successfully reproduced the profiles by placing transition metals at the (0, 0, 0) and (0, 0, 1/2) coordinates, which is similar to the DFT structures. The low concentrations of transition metals suggest the existence of large amounts of Li and H atoms along with transition metals.

Finite-temperature effects. The DFT lattice parameters summarized in Table 2 are slightly smaller than those determined from the XRD profiles measured at room temperature (4–10% smaller in volume), implying

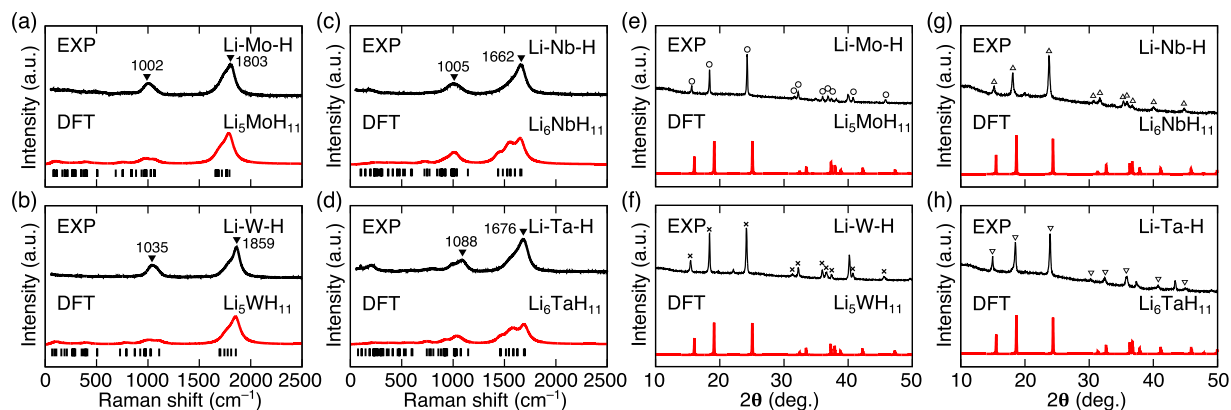


Figure 3. Raman spectra and X-ray diffraction (XRD) profiles. (a–d) Raman spectra. Experimental spectra (black lines) and DFT spectra (red lines) for $\text{Li}_5\text{MoH}_{11}$ (a), $\text{Li}_5\text{WH}_{11}$ (b), $\text{Li}_6\text{NbH}_{11}$ (c) and $\text{Li}_6\text{TaH}_{11}$ (d). All of the zone-centre optical phonon frequencies obtained from DFT calculations are represented by tick marks for reference. (e–h) XRD profiles. Experimental profiles (black lines) and simulated profiles from DFT structures (red lines) for $\text{Li}_5\text{MoH}_{11}$ (e), $\text{Li}_5\text{WH}_{11}$ (f), $\text{Li}_6\text{NbH}_{11}$ (g) and $\text{Li}_6\text{TaH}_{11}$ (h). The open circles, cross marks, open triangles and open upside-down triangles indicate the diffraction peaks correspond to $\text{Li}_5\text{MoH}_{11}$, $\text{Li}_5\text{WH}_{11}$, $\text{Li}_6\text{NbH}_{11}$ and $\text{Li}_6\text{TaH}_{11}$, respectively.

Sample	Space group	a (Å)	c (Å)
Li–Mo–H	$P6_3cm$ (185)	5.591(1) (5.351)	11.295(6) (11.035)
Li–W–H	$P6_3cm$ (185)	5.544(2) (5.357)	11.415(6) (11.038)
Li–Nb–H	$P6_3cm$ (185)	5.638(2) (5.482)	11.612(6) (11.420)
Li–Ta–H	$P6_3cm$ (185)	5.510(1) (5.484)	11.813(6) (11.401)

Table 2. Experimental lattice parameters determined by X-ray diffraction (XRD) measurements at room temperature. The corresponding density functional theory (DFT) lattice parameters are given in parentheses.

the presence of finite-temperature effects. As such, we examined the dynamics of the room-temperature phase of $\text{Li}_5\text{MoH}_{11}$ as an example using both first-principles molecular dynamics (FPMD) calculations in the isothermal–isobaric (NPT) ensemble at 298 K and neutron diffraction (ND) measurements at room temperature (strictly, ND measurements were performed on the deuteride analogue $\text{Li}_5\text{MoD}_{11}$).

In FPMD calculations, the two isolated H atoms (H2) isotropically fluctuate around their original positions determined by DFT calculations at 0 K, whereas the nine H atoms in the MoH_9 units (H1) rotate around the Mo atoms, generating spherical shell-like distribution, as illustrated in Fig. 4a. This type of rotational motion associated with anharmonic librations is acknowledged as leading to phase transitions in borohydrides³¹ and is thus expected to promote the volume expansion at room temperature. In fact, we observed a ~4% expansion (285 \AA^3) relative to the ground-state volume obtained by DFT calculations at 0 K (274 \AA^3), as shown in Fig. 4b. Additionally, the FPMD trajectory reasonably reproduces the experimental ND profile in Fig. 4c, as observed by the comparison of the simulated profile from the trajectory (red line in Fig. 4d) with the Rietveld refinement fit (black line in Fig. 4d), where the $P6cc$ structure (No. 184) with nine disordered D atoms surrounding the Mo atoms was employed, as shown in Fig. 4e, suggesting the adequacy of the current discussion. The experimentally determined structural parameters are summarized in Table 3.

Discussion

We have examined the possibility of the formation of novel transition metal hydride complexes with high H-coordination using a combined theoretical/experimental approach. All experimental data strongly point to the successful syntheses of a series of theoretically predicted complex transition metal hydrides $\text{Li}_5\text{MoH}_{11}$, $\text{Li}_5\text{WH}_{11}$, $\text{Li}_6\text{NbH}_{11}$ and $\text{Li}_6\text{TaH}_{11}$ containing ninefold H-coordination hydride complexes and two H^- anions. Our theoretical calculations reveal the σ -bonds of the nine H atoms forming the hydride complexes and the transition metals reach E_F in all synthesized materials.

Generally, the electronic structures of complex transition-metal hydrides can be viewed as comprising low-lying H 1s- and high-lying $T spd$ -derived states, as schematically depicted in Fig. 5. The ligand field induced by the H-coordination divides the $T spd$ states into the nonbonding and antibonding states (σ^* -bands), and E_F falls in the ligand-field gap to accommodate the so-called 18-electron rule. Therefore, the valence bands around E_F are normally dominated by the $T spd$ -derived nonbonding states (strictly, the $T d$ -derived nonbonding states); however, we emphasize here that the contribution from the H 1s-derived σ -bands in the valence bands increases with increasing H-coordination number, pushing the $T spd$ -derived states out of the valence bands and reaching E_F at ninefold coordination (Fig. 5). This is a novel strategy for obtaining solid-state covalently bonded hydrides with the H 1s-derived states reaching E_F .

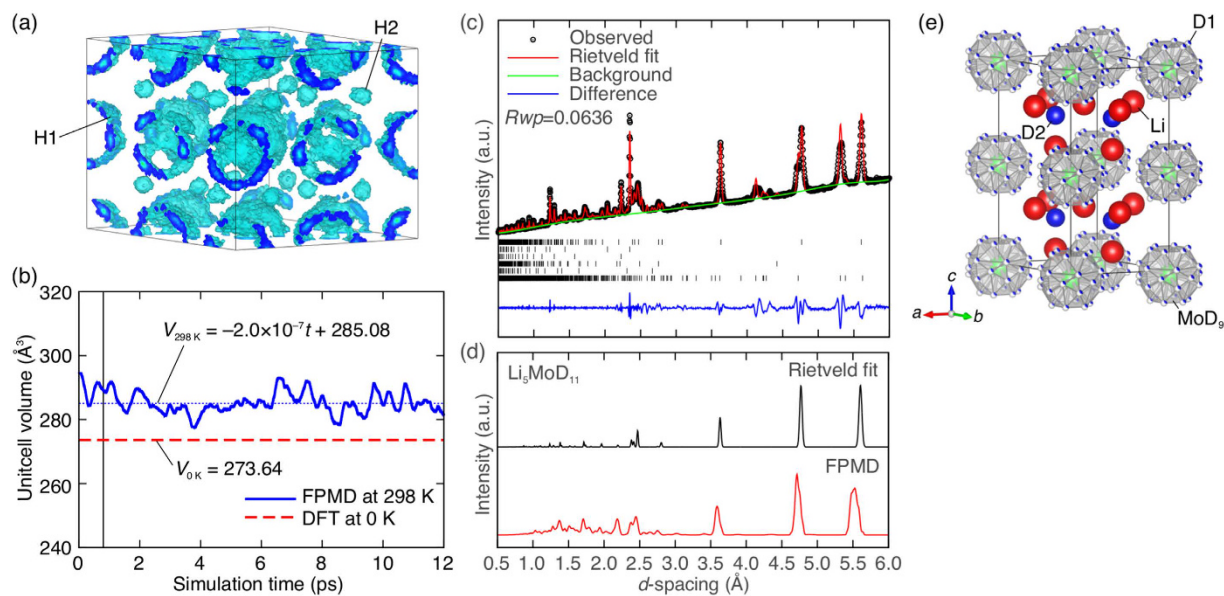


Figure 4. Finite-temperature effects in $\text{Li}_3\text{MoH}_{11}$. (a) The time-averaged atomic-density profile from the FPMD trajectory of H atoms at 298 K. (b) The time-dependent variation of unit cell volume from FPMD calculations at 298 K (blue line). The dashed blue line is obtained by the least-squares fitting of the volume change at 298 K over a range from 0.8 ps (vertical line) to 12 ps. The grand-state unit cell volume obtained by the DFT structure optimization at 0 K is plotted as a reference (dashed red line). (c) Experimental ND profile of $\text{Li}_3\text{MoD}_{11}$ measured at room temperature. The positions of Bragg reflection (tick marks) are shown for $\text{Li}_3\text{MoD}_{11}$ (top), LiD (second top), Mo (third top), Li₂O (third bottom), Li₂O (second bottom) and the unknown phase (bottom). The weight fractions of each phase excluding the unknown phase are $\text{Li}_3\text{MoD}_{11}$: 32(1) wt.%, LiD: 13(1) wt.%, Mo: 49(1) wt.%, LiOD: 3 wt.% and Li₂O: 3 wt.%. The weight fraction of LiOD and Li₂O are not allowed to refine. (d) Rietveld fit of experimental profile (black line) and simulated profile from FPMD trajectory at 298 K (red line). (e) Crystal structure of $\text{Li}_3\text{MoD}_{11}$ determined by Rietveld analysis.

Element	Wyckoff notation	x	y	z	occupancy	$100 \times U_{\text{iso}} (\text{Å}^2)$
Mo1	2a	0	0	-0.018(3)	1.0	4.0
Li1	4b	1/3	2/3	0.0780	1.0	1.0
Li2	6c	1/2	0	0.2943	1.0	1.0
D1	12d	0.3011(11)	0.0000(11)	-0.018(3)	0.3	3.77(27)
D2	12d	0.1819(11)	0.3546(9)	0.0234(30)	0.3	3.77(27)
D3	12d	0.1915(15)	0.0004(18)	0.1068(30)	0.3	3.77(27)
D4	12d	0.1819(11)	0.3546(9)	0.441(4)	0.3	3.77(27)
D5	12d	0.1915(15)	0.0004(18)	0.3569(30)	0.3	3.77(27)
D6	4b	1/3	2/3	0.2324(7)	0.3	2.62(28)

Table 3. Structural parameters of $\text{Li}_3\text{MoH}_{11}$ determined by neutron diffraction (ND) measurements at room temperature. The deuteride occurs in a hexagonal structure of space group $P6cc$ (No. 184) with lattice parameters $a = 5.5053(8) \text{ Å}$ and $c = 11.2095(19) \text{ Å}$. The isotropic temperature factor U_{iso} for Li and Mo are not allowed to refine.

As is well known, it is indispensable to have ‘ σ -bands’ of light elements at E_F to achieve high-critical-temperature (high- T_c) superconductivity within the Bardeen–Cooper–Schrieffer (BCS) theory³². For example, the relatively high T_c observed in MgB_2 ³³ is primarily attributed to the high-lying two-dimensional σ -bands derived from the in-plane B–B bonds, the holes of which strongly couple with the bond stretch phonons³⁴. Conversely, in all of the materials synthesized in this study, nine of the lightest H atoms form strong σ -bonds with transition metal elements, providing a DOS just below E_F . In this context, the occurrence of stronger electron–phonon coupling may be expected if the band gaps close under compression. From our preliminary calculations, we observed that there is at least one stable metallic phase of $\text{Li}_3\text{MoH}_{11}$ above 94 GPa (see Supplementary information).

Besides the electronic feature, these materials have a characteristic phonon property such that the ninefold hydride complexes exhibit rotational motions associated with anharmonic librations at room temperature. This type of motion has never been observed in the complex transition metal hydrides, but has often been discussed in relation to the occurrence of fast ion conduction in alkali metal dodecahydro-*closo*-dodecaborates such as $\text{Na}_2\text{B}_{12}\text{H}_{12}$. In this material, the first-order phase transition from the low-temperature monoclinic to the

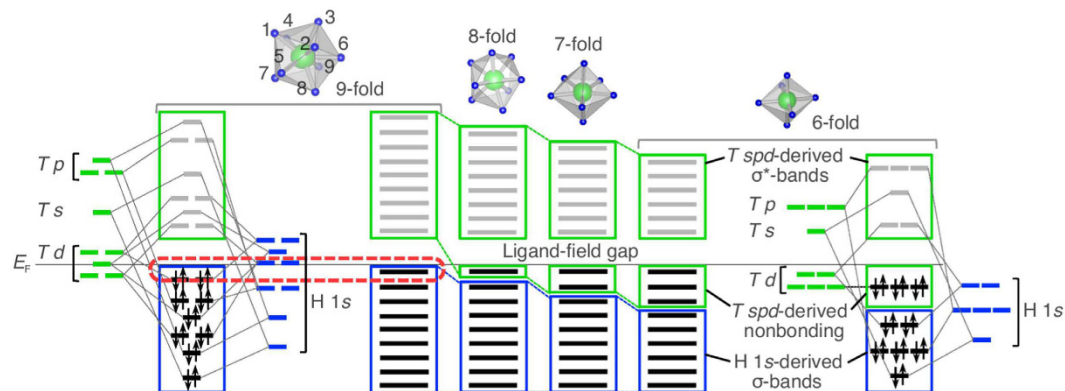


Figure 5. Strategy for obtaining complex transition-metal hydrides with H 1s-derived states reaching the Fermi level (E_F). The electronic structures roughly comprise low-lying H 1s- and high-lying $T spd$ -derived states. The contribution from H 1s-derived states to the valence bands increases with increasing H-coordination number and thus reaches E_F at ninefold H-coordination, as highlighted by the red dashed circle.

high-temperature cubic phase occurs near 520 K, which is accompanied by an increase of two orders of magnitude in the rate of reorientational jumps of the icosahedral $[B_{12}H_{12}]^{2-}$ anions with the fast translational diffusion of Na^+ ions³⁵. Although we observed no obvious translational diffusion of Li^+ ions in our FPMD calculations because of the limited simulation time (12 ps) and the unit cell size (136 atoms), the significant rotational motions of $[MoH_9]^{3-}$ ions, as observed in Fig. 4a, suggest the potential fast lithium ion conduction even at room temperature. It should be noted that given the quantum mechanical tunnelling of the H atoms, the rotational motions of hydride complexes may be sustained at extremely low temperature at which thermal diffusion is suppressed.

Although the hydride complexes with ninefold H-coordination were discovered in 1964¹⁸, they are very rare and their properties have not been fully clarified. Therefore, our findings will facilitate the discovery of latent functionalities, such as those described in this study and will lead to renewed interest in complex transition metal hydrides.

Methods

DFT calculations. The ground-state crystal structures of the Li–Mo–H, Li–W–H, Li–Nb–H and Li–Ta–H systems were explored using the structures of existing compounds as references. This exploration was performed using first-principles DFT calculations as implemented in the Vienna ab initio simulation package (VASP)^{36,37}. We used a plane-wave basis and the projector augmented wave method^{38,39} within the generalized gradient approximation with the Perdew–Burke–Ernzerhof exchange–correlation functional⁴⁰. For Li_5MoH_{11} , we assumed that the structure has a metal framework similar to that of $CaNi_5$ because of the similarity in their metal stoichiometries (Ca and Ni were replaced by Mo and Li, respectively, in the doubled $CaNi_5$ structure along the c -axis). We used nine H atoms (18 H atoms per formula unit) to coordinate the Mo atoms in the fashion of a tricapped trigonal prism, and placed two H atoms (four H atoms per formula unit) in the largest tetragonal site comprising four Li atoms. For Li_6NbH_{11} , an additional Li atom (two Li atoms per formula unit) was placed at the centre of the largest trigonal antiprism comprising six H atoms in Li_5MoH_{11} to accommodate the 6:1 stoichiometry between the Li and transition metals. We assumed that Li_5WH_{11} and Li_6TaH_{11} have isostructures to Li_5MoH_{11} and Li_6NbH_{11} , respectively. Next, full structure relaxations, including those for the lattice parameters, shapes and internal coordinates, were performed. Subsequently, phonon calculations were performed to verify that the relaxed structures were at the true minimum. When imaginary phonon frequencies were observed, we slightly displaced the atoms along the directions of the eigenvectors of the imaginary modes and further relaxed the structures to eliminate them. This procedure was performed until the ground state was reached. This was done using well-converged plane-wave basis sets with a cut-off energy of 800 eV. An $8 \times 8 \times 4$ grid was used for the k -point sampling of the Brillouin zone.

FPMD calculations. The room-temperature phase of Li_5MoH_{11} was examined using FPMD calculations in the NPT ensemble at 298 K with a $2 \times 2 \times 1$ supercell (136 atoms) of the primitive cell. We employed a well-converged cut-off energy of 600 eV with k -point sampling at the Γ -point. The simulation temperature was set to 298 K, which was controlled by a Langevin thermostat⁴¹ with a friction coefficient of 10 ps^{-1} for all atoms. The simulation pressure was controlled by a Parrinello–Rahman barostat^{42,43}, where a friction coefficient of 10 ps^{-1} were used for the lattice degrees of freedom. The total simulation time was 12 ps with a timestep of 0.5 fs.

Theoretical ND profile. The integrated time-of-flight (TOF) ND peak intensity $I(K_n)$ at the FPMD step n was calculated from the FPMD trajectory using the following equation:

$$I(K_n) = L(K_n) \left| \sum_j^{\text{unit cell}} b_j \exp(iK_n \cdot r_{j,n}) \right|^2, \quad (1)$$

where K_n is the reciprocal lattice vector, $L(K_n)$ is the Lorentz factor, b_j is the neutron-scattering length of atom j , and $r_{j,n}$ is the position of atom j . The ND profile was obtained by integrating the discrete ND peaks broadened by a Gaussian function with a width of 0.02 Å over a range from 0.8 fs to 12 ps, where the unit cell volume is well converged (see Fig. 4b).

Syntheses. High-purity metal powders of Mo (99.99%, Sigma-Aldrich), W (99.99%, Sigma-Aldrich), Nb (99.9%, Mitsuwa Chemicals Co., Ltd.) and Ta (99.9%, Mitsuwa Chemicals Co., Ltd.) were mixed with LiH (95%, Sigma-Aldrich) at molar ratios of 1:6 (Li–Mo–H and Li–W–H) and 1:8 (Li–Nb–H and Li–Ta–H) by mechanical milling at 400 rpm for 4 h under a 0.1-MPa Ar atmosphere. The mixtures were compacted into pellets (diameter and thickness = 1.0 mm) and encapsulated in sample capsules comprising pyrolytic boron nitride. The capsules were loaded together with a hydrogen source (AlH₃) into NaCl capsules, which were used to seal the hydrogen fluid that evolved from AlH₃. The NaCl capsules were pressurized to 5 GPa at room temperature using a multi-anvil high-pressure apparatus, followed by subsequent heating at 923 K (Li–Nb–H), 973 K (Li–Mo–H) and 1023 K (Li–W–H and Li–Ta–H) for 24 h (Li–W–H and Li–Ta–H) and 48 h (Li–Mo–H and Li–Nb–H). A similar procedure was used to synthesize the deuteride analogue Li₅MoD₁₁, where LiD and AlD₃ were used in place of LiH and AlH₃.

ND. Neutron scattering experiments of Li₅MoD₁₁ (41 mg) were performed for an exposure time of 8 h at room temperature under He on the NOVA high-intensity total diffractometer installed at the 500 kW spallation neutron source at the Materials and Life Science Experimental Facility (MLF) Japan Proton Accelerator Research Complex (J-PARC). The sample was filled in a cylindrical sample container with an external diameter of 3.0 mm and thickness of 0.1 mm. Rietveld analysis was performed using the General Structure Analysis System (GSAS) software and the graphical interface EXPGUI (version 1.80)⁴⁴ on the ND data, with $d = 0.25$ Å– 6.16 Å obtained at room temperature from detectors of medium resolution ($\Delta d/d \sim 0.6\%$) at the scattering angle $2\theta = 72^\circ$ – 108° . The profile function developed by Von Dreele *et al.*⁴⁵ was used for performing Rietveld analysis. The background was modeled using the 10-terms Chebyshev polynomial function model in GSAS. The distances of Mo–D in the complex anion [MoD₉]³⁻ and Li–D in the tetrahedral site in Li₅MoD₁₁ were soft constrained to 1.75 Å. The constraints were weighted such that they imposed only a minor deterioration of the fit to the experimental data. ND peaks of an unknown phase were indexed by a monoclinic unit cell with $a \approx 9.79$ Å, $b \approx 7.03$ Å, $c \approx 5.55$ Å and $\beta \approx 105.7^\circ$ using the indexing programs TREOR⁴⁶ and PIRUM⁴⁷. Based on hkl extinction rules, the space group for the unknown phase was predicted to be $P2_1/m$ (No. 11). Because it was not possible to determine the atomic positions in the unknown phase, Le Bail fitting was simultaneously performed for the unknown phase in Rietveld analysis.

References

1. Takagi, S. & Orimo, S. Recent progress in hydrogen-rich materials from the perspective of bonding flexibility of hydrogen. *Scripta Mater.* **109**, 1–5 (2015).
2. Orimo, S., Nakamori, Y., Eliseo, J. R., Züttel, A. & Jensen, C. M. Complex hydrides for hydrogen storage. *Chem. Rev.* **107**, 4111–4132 (2007).
3. Ashcroft, N. W. Hydrogen dominant metallic alloys: High temperature superconductors? *Phys. Rev. Lett.* **92**, 187002 (2004).
4. Eremets, M. I., Trojan, I. A., Medvedev, S. A., Tse, S. J. & Yao, Y. Superconductivity in hydrogen dominant materials: silane. *Science* **319**, 1506–1509 (2008).
5. Iimura, S. *et al.* Two-dome structure in electron-doped iron arsenide superconductors. *Nat. Commun.* **3**, 943 (2012).
6. Drozdov, A. P., Eremets, M. I., Troyan, I. A., Ksenofontov, V. & Shylin, S. I. Conventional superconductivity at 203 kelvin at high pressures in the sulfur hydride system. *Nature* **525**, 73–76 (2015).
7. Matsuo, M. & Orimo, S. Lithium fast-ionic conduction in complex hydrides: Review and prospects. *Adv. Energy Mater.* **1**, 161–172 (2011).
8. Tassel, C. *et al.* Direct synthesis of chromium perovskite oxyhydride with a high magnetic-transition temperature. *Angew. Chem. Int. Ed.* **53**, 10377–10380 (2014).
9. Huiberts, J. N. *et al.* Yttrium and lanthanum hydride films with switchable optical properties. *Nature* **380**, 231–234 (1996).
10. Yvon, K., Renaudin, G., Wei, C. M. & Chou, M. Y. Hydrogenation-induced insulating state in the intermetallic compound LaMg₂Ni. *Phys. Rev. Lett.* **94**, 066403 (2005).
11. Ginsberg, A. P. Transition metal-hydrogen compounds. III. dipotassium enneahydridotechnate(VII). *Inorg. Chem.* **3**, 567–569 (1964).
12. Knox, K. & Ginsberg, A. P. X-ray determination of the crystal structure of potassium rhenium hydride. *Inorg. Chem.* **3**, 555–558 (1964).
13. Abrahams, S. C., Ginsberg, A. P. & Knox, K. Transition metal-hydrogen compounds. II. The crystal and molecular structure of potassium rhenium hydride, K₂ReH₉. *Inorg. Chem.* **3**, 558–567 (1964).
14. Ginsberg, A. P. Transition metal-hydrogen compounds. IV. Improved synthesis of enneahydridorhenates: the sodium and tetraethylammonium salts of ReH₉²⁻. *Inorg. Chem.* **8**, 2212–2214 (1969).
15. Bronger, W. Complex transition metal hydrides. *Angew. Chem. Int. Ed.* **30**, 759–768 (1991).
16. Stetson, N. T. & Yvon, K. On the structure of the complex hydride BaReH₉. *Inorg. Chem.* **33**, 4598–4599 (1994).
17. Stetson, N. T. & Yvon, K. Structure of KNaReH₉ by single crystal x-ray diffraction and infrared spectroscopy. *J. Alloys Compd.* **223**, L4–L6 (1995).
18. Yvon, K. Complex transition-metal hydrides. *CHIMIA* **52**, 613–619 (1998).
19. Takagi, S. *et al.* Unusual sevenfold coordination of ru in complex hydride Na₃RuH₇: Prospect for formation of [FeH₇]³⁻ anion. *Appl. Phys. Lett.* **103**, 113903 (2013).
20. Miwa, K., Takagi, S., Matsuo, M. & Orimo, S. Thermodynamical stability of complex transition metal hydrides M₂FeH₆. *J. Phys. Chem. C* **117**, 8014–8019 (2013).
21. Matsuo, M. *et al.* Formation of an Fe–H complex anion in YFe₂: adjustment of imbalanced charge by using additional Li as an electron donor. *RSC Adv.* **3**, 1013–1016 (2013).
22. Saitoh, H. *et al.* Li₄FeH₆: Iron-containing complex hydride with high gravimetric hydrogen density. *APL Mater.* **2**, 076103 (2014).
23. Takagi, S., Humphries, T. D., Miwa, K. & Orimo, S. Enhanced tunability of thermodynamic stability of complex hydrides by the incorporation of H⁻ anions. *Appl. Phys. Lett.* **104**, 203901 (2014).

24. Humphries, T. D. *et al.* Complex transition metal hydrides incorporating ionic hydrogen: Synthesis and characterization of $\text{Na}_2\text{Mg}_2\text{FeH}_8$ and $\text{Na}_2\text{Mg}_2\text{RuH}_8$. *J. Alloys Compd.* **645**, S347–S352 (2015).
25. Takagi, S. *et al.* True boundary for the formation of homoleptic transition-metal hydride complexes. *Angew. Chem. Int. Ed.* **54**, 5650–5653 (2015).
26. Takagi, S. *et al.* Density-functional study of perovskite-type hydride LiNiH_3 and its synthesis: Mechanism for formation of metallic perovskite. *Phys. Rev. B* **87**, 125134 (2013).
27. Veleckis, E. & Edwards, R. K. Thermodynamic properties in the systems vanadium-hydrogen, niobium-hydrogen, and tantalum-hydrogen. *J. Phys. Chem.* **73**, 683–692 (1969).
28. Wenzl, H. Properties and applications of metal hydrides in energy conversion systems. *Int. Metals Rev.* **27**, 140–168 (1982).
29. Singh, D. J., Gupta, M. & Gupta, R. Cohesion of BaReH_5 and BaMnH_5 ; Density functional calculations and prediction of $(\text{MnH}_9)^{2-}$ salts. *Phys. Rev. B* **75**, 035103 (2007).
30. Miwa, K. Prediction of raman spectra with ultrasoft pseudopotentials. *Phys. Rev. B* **84**, 094304 (2011).
31. Hagemann, H., Filinchuk, Y., Chernyshov, D. & van Beek, W. Lattice anharmonicity and structural evolution of LiBH_4 : an insight from raman and X-ray diffraction experiments. *Phase Transit.* **82**, 344–355 (2009).
32. Fukuyama, H. High-temperature superconductivity by transforming bonds into bands. *J. Supercond. Novel Magn.* **19**, 201–202 (2006).
33. Nagamatsu, J., Nakagawa, N., Muranaka, T., Zenitani, Y. & Akimitsu, J. Superconductivity at 39 K in magnesium diboride. *Nature* **410**, 63–64 (2001).
34. An, J. M. & Pickett, W. E. Superconductivity of MgB_2 : Covalent bonds driven metallic. *Phys. Rev. Lett.* **86**, 4366–4369 (2001).
35. Skripov, A. V. *et al.* Nuclear magnetic resonance study of atomic motion in $a_2\text{B}_{12}\text{H}_{12}$ ($a = \text{Na, K, Rb, Cs}$): Anion reorientations and Na^+ mobility. *J. Phys. Chem. C* **117**, 25961–25968 (2013).
36. Kresse, G. & Hafner, J. Ab initio molecular dynamics for liquid metals. *Phys. Rev. B* **47**, R558–R561 (1993).
37. Kresse, G. & Furthmüller, J. Efficient iterative schemes for ab initio total-energy calculations using a plane-wave basis set. *Phys. Rev. B* **54**, 11169–11186 (1996).
38. Blöchl, P. E. Projector augmented-wave method. *Phys. Rev. B* **50**, 17953–17979 (1994).
39. Kresse, G. & Joubert, D. From ultrasoft pseudopotentials to the projector augmented-wave method. *Phys. Rev. B* **59**, 1758–1775 (1999).
40. Perdew, J. P., Burke, K. & Ernzerhof, M. Generalized gradient approximation made simple. *Phys. Rev. Lett.* **77**, 3865–3868 (1996).
41. Allen, M. P. & Tildesley, D. J. *Computer Simulation of Liquids* (Oxford University Press, New York, 1991).
42. Parrinello, M. & Rahman, A. Crystal structure and pair potentials: A molecular-dynamics study. *Phys. Rev. Lett.* **45**, 1196–1199 (1980).
43. Parrinello, M. & Rahman, A. Polymorphic transitions in single crystals: A new molecular dynamics method. *J. Appl. Phys.* **52**, 7182–7190 (1981).
44. Toby, B. H. EXPGUI, a graphical user interface for GSAS. *J. Appl. Crystallogr.* **34**, 210–213 (2001).
45. Von Dreele, R. B., Jorgensen, J. D. & Windsor, C. G. Rietveld refinement with spallation neutron powder diffraction data. *J. Appl. Crystallogr.* **15**, 581–589 (1982).
46. Werner, P.-E., Eriksson, L. & Westdahl, M. TREOR, a semi-exhaustive trial-and-error powder indexing program for all symmetries. *J. Appl. Crystallogr.* **18**, 367–370 (1985).
47. Werner, P.-E. A fortran program for least-squares refinement of crystal-structure cell dimensions. *Ark. Kemi.* **31**, 513–516 (1969).

Acknowledgements

We are grateful for helpful discussions with K. Aoki, technical support from R. Hiraoka and H. Omiya, and the use of the SR16000 supercomputing resources at the Center for Computational Materials Science of the Institute for Materials Research, Tohoku University. The neutron scattering experiment was approved by the Neutron Scattering Program Advisory Committee of IMSS, KEK (Proposal No. 2014S06). The high-pressure hydrogenation technique was developed by using synchrotron radiation X-rays at BL14B1, SPring-8 (Proposal No. 2014B3602). This work was supported by JSPS KAKENHI (Grant Numbers 16H06119, 25220911, 16K06766 and 25420725), the Photon and Quantum Basic Research Coordinated Development Program by MEXT and Collaborative Research Center on Energy Materials in IMR (E-IMR).

Author Contributions

S.T. conceived this study, performed the theoretical calculations, analysed the data and wrote the manuscript. Y.I. prepared the samples with immense help from H.S. and performed the XRD and Raman measurements. T.S. analysed the XRD data and prepared AlH_3 . K.I. and T.O. performed the ND measurements. T.I. provided significant help in analysing the data. K.M. calculated the theoretical Raman spectra. S.O. designed and conducted the project. All authors commented on the final manuscript and conclusions of this work.

Additional Information

Supplementary information accompanies this paper at <http://www.nature.com/srep>

Competing Interests: The authors declare no competing financial interests.

How to cite this article: Takagi, S. *et al.* Formation of novel transition metal hydride complexes with ninefold hydrogen coordination. *Sci. Rep.* **7**, 44253; doi: 10.1038/srep44253 (2017).

Publisher's note: Springer Nature remains neutral with regard to jurisdictional claims in published maps and institutional affiliations.



This work is licensed under a Creative Commons Attribution 4.0 International License. The images or other third party material in this article are included in the article's Creative Commons license, unless indicated otherwise in the credit line; if the material is not included under the Creative Commons license, users will need to obtain permission from the license holder to reproduce the material. To view a copy of this license, visit <http://creativecommons.org/licenses/by/4.0/>

© The Author(s) 2017